Erasure-cooling, control, and hyper-entanglement of motion in optical tweezers

Pascal Scholl,[1,*,†] Adam L. Shaw,[1,*] Ran Finkelstein,[1,*] Richard Bing-Shiun Tsai,[1] Joonhee Choi,[1,2] and Manuel Endres[1,‡]

[1] *California Institute of Technology, Pasadena, CA 91125, USA*
[2] *Department of Electrical Engineering, Stanford University, Stanford, CA, USA*

We demonstrate how motional degrees of freedom in optical tweezers can be used as quantum information carriers. To this end, we first implement a species-agnostic cooling mechanism via conversion of motional excitations into erasures – errors with a known location – reminiscent of Maxwell's demon thought experiment. We find that this cooling mechanism fundamentally outperforms idealized traditional sideband cooling, which we experimentally demonstrate in specific scenarios. By coherently manipulating the motional state, we perform mid-circuit readout and mid-circuit erasure detection of an optical qubit via local shelving into motional superposition states. We finally entangle the motion of two atoms in separate tweezers, and utilize this to generate hyper-entanglement by preparing a simultaneous Bell state of motional and optical qubits. This work shows how controlling motion enriches the toolbox of quantum information processing with neutral atoms, and opens unique prospects for metrology enhanced by mid-circuit readout and a large class of quantum operations enabled via hyper-entanglement.

The ability to store, carry, and manipulate quantum information is essential to the success of quantum science applications, ranging from fault-tolerant quantum computing[1,2] to entanglement-enhanced metrology[3], or quantum communication[4] and cryptography[5]. Over the last few years, tremendous efforts have been pursued in a wide array of quantum platforms to develop efficient quantum information carriers[6–10]. In particular, for neutral atom based platforms, quantum information has so far been encoded in electronic or nuclear states[11–14], the manipulation of which is often limited by atomic thermal motion[15–18].

However, this very same motion can be in principle used to encode and store quantum information. The motion of atoms trapped in nearly-harmonic potentials, such as optical tweezers, is quantized[19,20], and acts essentially as a bosonic degree of freedom, similarly to auxiliary bosonic states in ion traps[21,22] and superconducting circuits[23,24]. Recent experiments exploiting this resource have demonstrated squeezing of motional states[19] and creation of a quantum register of fermion pairs[20]. Unlike electronic or nuclear states, motional states do not interact directly with electromagnetic fields and are thus robust to environmental effects[25]. Further, their bosonic nature may be used to implement quantum error correction schemes with bosonic degrees of freedom such as Gottesman-Kitaev-Preskill (GKP) codes[26,27], or as a resource for studying lattice gauge theories[28,29].

Motional states can be independent from electronic or nuclear states, and information could be in principle manipulated in each of the four degrees of freedom independently: one degree of freedom for internal states, and three for motional states corresponding to the three trap axes. Therefore, multiple bits of quantum information could be independently encoded into a single atom, and atoms could be entangled through two or more degrees of freedom, a feature called *hyper-entanglement*[30–32]. Such a capability would open the door to various applications such as hyper-parallel quantum computation[30], entanglement purification[31,33], or superdense coding[34,35]. Further, hyper-entanglement could be used to implement two-copy interference protocols[36] using a single system, where one copy is encoded in motional states, and the other one in the electronic degree of freedom. However, to realize these advantages first requires efficient cooling to prepare the atoms in their motional ground state with high fidelity.

Here we demonstrate a new species-agnostic technique to efficiently prepare motional ground state atoms, and use this resource to show the potential of motional states to enable key tasks in quantum information processing (Fig. 1A). Our new cooling mechanism is reminiscent of the Maxwell's demon thought experiment, and relies on (i) conversion of motional excitations into detectable, localized errors[37], also called *erasures*[38,39], and (ii) their active correction. Using such a technique, we obtain a motional ground state occupation of 0.984^{+4}_{-5}, increased to 0.995^{+3}_{-4} if post-selection is used rather than active correction. Such erasure conversion techniques have only been recently implemented in optical tweezers to improve quantum simulation and computation tasks, and only on nuclear or optical transitions[14,40]. Importantly, we find this new cooling scheme systematically outperforms traditional sideband cooling, which we demonstrate experimentally in the case of shallow tweezers by comparing our results to simulations of an idealized sideband cooling process.

Building from this efficient preparation of arrays of motional ground state atoms, we demonstrate key tasks in quantum information processing. We first demon-

* These authors contributed equally to this work.
† Current affiliation: PASQAL, 7 rue Léonard de Vinci, 91300 Massy, France
‡ mendres@caltech.edu

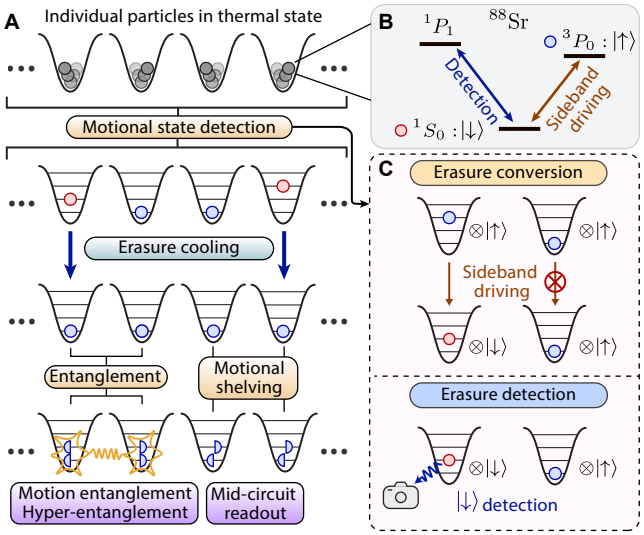

Fig. 1 | Scheme for erasure cooling, coherent manipulation, and entanglement of motional states. **A,** Sketch describing how motional degrees of freedom in optical tweezers can be used as quantum information carriers. We first initialize the atoms in their motional ground state using a new cooling mechanism based on motional state error-correction. With such a low-entropy state at hand, we subsequently demonstrate (i) the use of a coherent superposition of motional states to perform mid-circuit readout of an optical qubit, and (ii) motion-entanglement as well as hyper-entanglement: simultaneous spin-entanglement and motion-entanglement. **B,** Relevant pseudo-spin levels, and detection transition used in this work. **C,** Protocol to detect the atom's motional state. We first convert motional excitation errors into erasure errors, i.e., errors with a known location[38,39]. We accomplish this by selectively transferring motion-excited atoms to the electronic ground state, $^1S_0$ (red), whilst motional ground state atoms are shelved in $^3P_0$ (blue). We then selectively detect atoms in $^1S_0$, which does not perturb atoms in $^3P_0$.

strate coherent transduction of electronic superposition states into the two lowest energy motional states along a single tweezer axis, with a one-way fidelity of 0.993^{+3}_{-3}, post-selected on erasure detection. We then combine this with local addressing via selective trap depth control[42] in order to perform mid-circuit readout of a tweezer array[25,43–46]. To our knowledge, this is the first such demonstration on an optical transition; furthermore, it relies only on local tweezer depth control, and does not require multiple species[25], nuclear states[45,46], or a cavity[43]. Importantly, as part of this study, we also demonstrate mid-circuit erasure detection[14], utilizing metastable motional state superpositions which have a coherence time much longer than our mid-circuit detection time.

We then extend these key tasks beyond the single-particle regime by entangling the motion of two atoms in separate tweezers through Rydberg interactions[12,47], while leaving their electronic degrees of freedom separable. Finally, we show the first demonstration of hyper-entanglement[30,31] in matter-based qubits by creating a Bell state both in the motional and electronic degrees of freedom simultaneously. While these results utilize only the two lowest energy states of a single motional tweezer axis, our techniques are generalizable to control over the entire motional manifold of the three motional axes.

Erasure correction cooling

To start, we describe our cooling scheme, which we term *erasure correction cooling* (ECC). The basic principle relies on detecting atoms in motion-excited states, while shelving motion-ground state atoms such that they are not disturbed by measurement. From there, motional excitations can either be removed, or selectively re-cooled. The results presented here concern the tightly-confined, radial direction of the optical tweezers; we also implemented ECC along the weakly-confining, axial direction, for which we find similar results[41].

Our experiment[41,47] is based on trapping individual strontium atoms in arrays of optical tweezers[41,48,49] (Fig. 1A,B). Atoms are initialized in their ground electronic state $^1S_0$ and initially cooled with Sisyphus cooling (a conventional form of laser cooling) to an initial motional ground state population of $P_0' = 0.77^{+1}_{-1}$. To perform ECC, we convert remaining motional excitations into erasure errors[38,39] (Fig. 1C) by working in the *sideband resolved* regime on the transition between $^1S_0$ and the metastable excited state $^3P_0$. The trapping wavelength is 813 nm to achieve a magic trapping condition for $^1S_0$ and $^3P_0$.

We note that in all of the following, we will consider a single motional degree of freedom, which is defined along the $^1S_0 \leftrightarrow {}^3P_0$ laser beam propagation axis. We use numerical notation for motional states (e.g. $|0\rangle$ for the motional ground state), and pseudo-spin notation for electronic states (e.g. $|\downarrow\rangle$ is $^1S_0$ and $|\uparrow\rangle$ is $^3P_0$); for the latter we will use the terms spin, electronic state, and optical qubit interchangeably. We further denote their tensor product as e.g. $|0\rangle \otimes |\uparrow\rangle = |0,\uparrow\rangle$.

Erasure correction cooling then proceeds with the following steps (Fig. 2A,B): first we drive all atoms into the excited electronic state using the motion-preserving *carrier* transition, $|n,\downarrow\rangle \rightarrow |n,\uparrow\rangle$, where n is an arbitrary motional level. Second, we perform a spin-motion coupling *sideband* transition, $|n,\uparrow\rangle \leftrightarrow |n-1,\downarrow\rangle$, ideally leaving only motional ground state atoms in the excited electronic state. We then perform fluorescence imaging of the ground electronic state, while leaving atoms in $|0,\uparrow\rangle$ unperturbed[40]. This means that we directly image the location of motion-excited atoms, for which we can then perform error correction.

This correction can be done in two ways (Fig. 2C), either: (1) *Reset*, where we reapply Sisyphus cooling with site-selectivity[41], or (2) *Replacement*, by discarding hot atoms and replacing them with cold atoms using atom rearrangement[50,51]. At the end of the correction, we transfer any remaining atom in $|\downarrow\rangle$ to $|\uparrow\rangle$ using optical pumping[47] to avoid any vacancy defects in the array. To assess the efficacy of ECC, we use a 39-

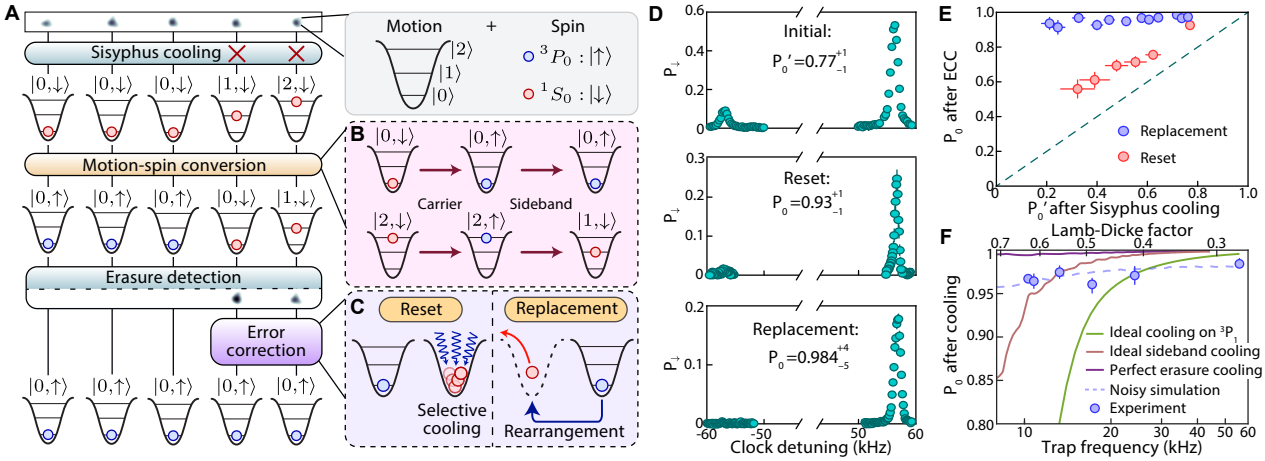

Fig. 2 | Improving motional ground state preparation with erasure correction cooling. A,B, After cooling the atoms with Sisyphus cooling, we apply spin-motion conversion, which leaves atoms in a different pseudo-spin state depending on whether they do or do not have motional excitations, as shown explicitly for the initial states $|2,\downarrow\rangle$ and $|0,\downarrow\rangle$ in **B**. We then detect atoms with motional excitations by imaging the pseudo-spin state $|\downarrow\rangle$, without perturbing atoms in the motional ground state, which reside in $|\uparrow\rangle$. **C,** We correct tweezers containing atoms with motional excitations in two different ways: (i) by reapplying Sisyphus cooling selectively on such atoms (reset), or (ii) by replacing such atoms using rearrangement (replacement). **D,** Probability, P_0, for an atom to be in the motional ground state, $|0\rangle$, measured via sideband spectroscopy. We show the results without erasure correction cooling, performing erasure correction with reset, and erasure correction with replacement. **E,** Post-correction motion-ground state probability, P_0, as a function of intentionally varied motion-ground state probability after Sisyphus cooling, P_0'. We show the results for both replacement (blue markers) and reset (red markers). The replacement method is largely insensitive to the Sisyphus cooling efficiency. The green dashed line is a guide to the eye which represents unity gain. **F,** P_0 as a function of the trap frequency ω. Our experimental erasure cooling results (blue markers) using the replacement method are in good agreement with an *ab initio* error model including known imperfections (blue dashed line). We compare against two variants of sideband cooling, one using the $^3P_1$ state of strontium (green line), and one which is an idealization representing the ultimate limit of sideband cooling for given trap and Rabi frequencies, and Lamb-Dicke factor[41]. Our experimental erasure cooling outperforms both sideband cooling variants in the regime of low trap frequency, and an error-free simulation of erasure cooling is superior to sideband cooling for all frequencies. Error bars represent the standard error of the mean.

tweezer array, and measure P_0 via sideband spectroscopy on the $|\downarrow\rangle \rightarrow |\uparrow\rangle$ transition (Fig. 2D). Starting from $P_0' = 0.77^{+1}_{-1}$ after Sisyphus cooling, we obtain a final motional ground state population $P_0 = 0.93^{+1}_{-1}$ with one round of reset, and $P_0 = 0.984^{+4}_{-5}$ with replacement. The maximum P_0 after reset is limited here by only doing one round of cooling, with a theoretical maximum of $P_0 = P_0' + (1 - P_0')P_0' \approx 0.95$. In Fig. 2E we show the efficacy of ECC as a function of P_0' obtained after Sisyphus cooling (allowing up to 3 rounds of reset cooling for the lowest P_0' values); in general we find that ECC with replacement is especially insensitive to this initial cooling temperature. If we post-select on erasure detection, rather than applying active correction, we achieve $P_0 = 0.995^{+3}_{-4}$.

Having demonstrated the efficacy of ECC for our particular experimental realization, we now show that it outperforms even idealized, noise-free, conventional laser cooling in certain realistic parameter regimes (Fig. 2F). We first perform a noise-free simulation[41] of ECC (purple line), and compare it against two possible realizations of ideal sideband cooling. The first is against cooling on the commonly used $^1S_0 \rightarrow {}^3P_1$ intercombination line[48,49] (green line), while the second is against idealized sideband cooling performed with infinitely small linewidth (red line), but including an effective spontaneous decay in order to remove entropy from the system[41,52].

We observe that across all trap frequencies, the idealized ECC always outperforms idealized sideband cooling, but particularly so in the limit of low trap depth, where the sideband-resolved condition ($\omega \gg \Gamma$) breaks down. In this limit, sideband cooling efficiency becomes limited by (i) the finite Rabi frequency (here $2\pi \times 2.5\,\mathrm{kHz}$) used to cool the atoms, and (ii) photon recoil. Conversely, ECC is (i) less sensitive to errors coming from the finite Rabi frequency because they can be partially erased[41], and (ii) not limited by photon recoil since cooling does not rely on spontaneous emission from a cooling state. Instead, ECC is primarily limited by tweezer-induced heating during error correction, as seen in both experimental (blue points) and *ab initio* error model results (dashed line) accounting for known noise sources[41]. Importantly, for $\omega/(2\pi) \lesssim 24\,\mathrm{kHz}$, the experimental ECC implementation outperforms sideband cooling on $^1S_0 \rightarrow {}^3P_1$, and outperforms even the idealized sideband cooling for $\omega/(2\pi) \lesssim 12\,\mathrm{kHz}$.

We stress that this regime of relatively low trap frequency is particularly relevant for the tweezers' weakly confining, axial direction. Furthermore, whilst a high

trap frequency enables large sideband-cooling efficiency, it also limits the achievable number of physical qubits for a fixed laser power. Our results demonstrate that the same cooling can be achieved practically at a much lower trap depth, potentially opening the door to greatly expanding the size of tweezer arrays.

Our scheme for erasure correction cooling (i) presents a practical advantage in cooling efficiency for our setup, and (ii) can outperform sideband cooling in general, which we demonstrated experimentally in the regime of low trap frequency.

Preparing motional superposition states

Now that we have demonstrated our ability to obtain motional ground state atoms with high fidelity thanks to erasure correction cooling, we detail how we make use of this low-entropy atom array for quantum information purposes. Assuming perfectly harmonic trapping, the manifold of motional states for a single principal axis acts as a bosonic degree of freedom with an infinite ladder of states. For the remainder of the paper, we will focus on the case of controlling only a single motional degree of freedom, and in particular focus on the lowest two levels, which we refer to as the *motional qubit*. The isolation of these two motional states is achieved due to driving sideband transitions which only couple the motional ground state to the first excited state, and therefore higher energy levels are not populated. Extensions of our scheme and results are readily generalized to control over all three axes, and to control over higher energy states in the motional manifold, which may enable various new applications[27] not explored directly in this work. We will use a trap frequency (equivalently, motional qubit energy spacing) of $\omega/(2\pi) \simeq 35.5\,\mathrm{kHz}$.

We first show the preparation of a coherent superposition state of the motional qubit via transduction from an optical qubit (Fig. 3A). Essentially, the preparation and readout of this state is a form of Ramsey interrogation, with the addition of spin-motion coupling inserted into the Ramsey dark time. We first perform ECC to isolate atoms in $|0,\uparrow\rangle$. We then form a spin-superposition state by performing a $\pi/2$ pulse on the carrier, and transduct this superposition onto the motional qubit by performing spin-motion coupling via sideband driving. This yields the state $|+,0\rangle = \frac{1}{\sqrt{2}}(|0\rangle+|1\rangle)\otimes|\uparrow\rangle$. We then leave this state unperturbed for a duration τ during which it will evolve coherently, and then read its state by reversing the sideband and carrier driving.

We plot the resultant signal, given as the probability $P_\downarrow$ for the atom be in $|\downarrow\rangle$ after the entire sequence (Fig. 3B). We observe Ramsey oscillations at a frequency of $35.3^{+0.3}_{-0.3}\,\mathrm{kHz}$, consistent with the programmed trap frequency, as is expected for the motional qubit.

Importantly, after the transduction, a coherent motional qubit state is sensitive to dephasing largely only from noise on the trapping laser *power* (which controls the relative qubit energy spacing). This is in contrast to optical qubits, which may dephase due to noise on the addressing laser *frequency*, often limiting the coherence time for optical qubits based on ultranarrow transitions[53]. We demonstrate this insensitivity by fixing $\tau = 100\,\mu\mathrm{s}$, and then vary the laser phase between each preparation or readout pulse (Fig. 3C). We observe that $P_\downarrow$ is apparently insensitive to laser phase variation between the two sideband pulses (green points), while the atom is in a motional superposition state. By contrast, significant sensitivity is observed with respect to phase variation between the carrier and sideband pulses (red and blue points and lines), as during that time the atom is in a sensitive optical superposition state. In practice, however, the time between the carrier and sideband pulses is short enough to avoid significant dephasing.

Thus, our results show that motional levels can be used to store information in a subspace that is insensitive to phase noise[15] on the laser which drives the optical qubit transition. Other extrinsic noise sources, such as environmental magnetic and electric field noise should behave similarly, assuming they minimally affect the trap frequency. This overall insensitivity makes the demonstrated motional qubit a promising storage subspace for quantum information, which we discuss in the following.

Mid-circuit readout with motional state shelving

Having demonstrated our capability to prepare motion-superposition states, we now show that this can be used to perform mid-circuit readout[25,43–46] (Fig. 3D), which is a necessary step in error correcting codes[54], and which enables various near term applications such as measurement-based generation of long-range entangled states[55,56] and enhanced metrology[57].

To do so, we first divide the atom array into two ensembles A and B. We apply a global carrier $\pi/2$ pulse on both ensembles to prepare the $|0,+\rangle$ state. We then selectively lower the trap depths in B, while holding A constant[42]. This induces a reduction in trap frequency for atoms in B, and thus changes the motional qubit energy spacing. We can then selectively apply sideband driving only to the ensemble B, hence transferring only atoms in B into the $|+,\uparrow\rangle$ state[42], leaving A largely unperturbed[41].

We then apply a global, fast detection of atoms in the electronic ground state[40], which projects the spin state of atoms in A, while preserving the coherence of atoms in B. We finally unshelve atoms in B, and read out their coherence (Fig. 3E). The shelving and unshelving procedure is designed to apply a motional echo composed of four sideband pulses in order to eliminate shot-to-shot fluctuations of the trap depth[41]. We obtain a bare contrast of 0.79^{+1}_{-1} after performing these four sideband pulses, which corresponds to a state preparation and measurement (SPAM) corrected[41] one-way, optical-to-motion transduction fidelity of 0.943^{+3}_{-3}. This fidelity can be further improved thanks to erasure conversion of atoms in B. If the transduction fails, then atoms in B are detected during the fast image, which we then excise to obtain an overall contrast of 0.972^{+10}_{-10} which corresponds to a one-way transduction fidelity[41] of 0.993^{+3}_{-3}. We note that as the fast image has negligible impact on the coher-

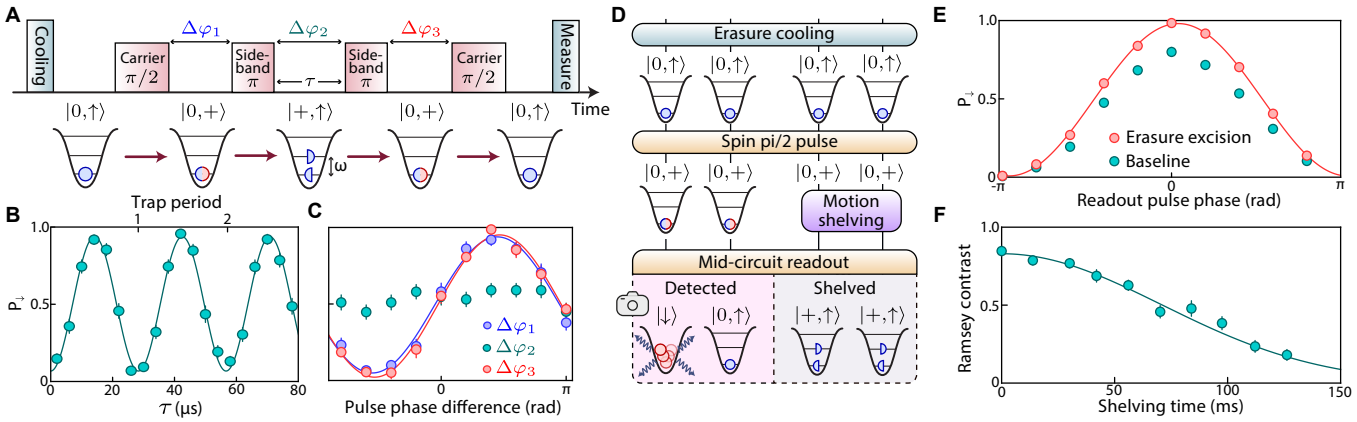

Fig. 3 | Spin-motion transduction and mid-circuit readout. A, Sketch of the protocol used to transfer a coherent superposition of pseudo-spin states into a superposition of motional states. After cooling the atoms and preparing the spin-superposition state $|0,+\rangle$, we apply a sideband pulse which drives the $|0,\downarrow\rangle \rightarrow |1,\uparrow\rangle$ transition, allowing us to obtain the motion-superposition state $|+,\uparrow\rangle$. We then revert the process in order to read out the coherence of the created state. **B,** Probability to obtain the atom in $|\downarrow\rangle$ as a function of holding time in $|+,\uparrow\rangle$. We observe an oscillation with frequency $35.3^{+0.3}_{-0.3}$ kHz, consistent with our trapping frequency $\omega/(2\pi) \simeq 35.5$ kHz. **C,** Probability to obtain the atom in $|\downarrow\rangle$ as a function of the phase difference between the pulses in **A**. The atom is sensitive to the laser phase while in a pseudo-spin superposition state. However, when in the motion-superposition state $|+,\uparrow\rangle$, the atom is not sensitive to the laser phase, and is hence insensitive to laser phase noise. **D,** Sketch showing local pseudo-spin coherence preservation using motional state shelving. We prepare the $|0,+\rangle$ state and locally shelve some atoms into $|+,\uparrow\rangle$ by lowering their trap depth[42] and applying site-selective sideband drive. We detect atoms in $|\downarrow\rangle$ to project the unshelved atoms into $|\downarrow\rangle$ or $|\uparrow\rangle$. The shelved atoms are not affected by the detection, hence the coherence is preserved within the motional states. **E,** Obtained pseudo-spin coherence for the shelved atoms after the sequence described in **D**. We obtain a bare one-way transduction fidelity of 0.943^{+3}_{-3}, further increased to 0.993^{+3}_{-3} with erasure detection and excision[41]. **F,** Motional coherence in an echo sequence[41] as a function of shelving time. We obtain a typical $1/e$ coherence time of ~ 100 ms, which is long compared to our fast detection time of 24 μs. Error bars represent the standard error of the mean.

ence of motional states in B, this protocol demonstrates *mid-circuit* erasure detection which has only been recently demonstrated with ytterbium atoms in neutral atom systems[14].

We measure the coherence time of the motional states for atoms in B (Fig. 3F) using a motion-echo sequence[41], and obtain a typical $1/e$ time of $\sim$100 ms, which is long compared to our imaging time of 24 μs using our fast detection scheme[40]. This coherence time is thought to be limited by tweezer-induced Rayleigh scattering[41] and tweezer intensity fluctuations; we expect these results should be improvable by using better stabilization techniques, although we leave such a study to future work.

These high transduction fidelities, combined with the relatively long motional state coherence time as compared to coherent manipulation and detection duration, make this new shelving method an appealing alternative to other recently demonstrated schemes for mid-circuit detection in tweezer-based platforms[25,43–46]. As opposed to other schemes, our method does not require any specific electronic or nuclear structure, besides the presence of a sideband resolved transition, and is applicable for alkaline-earth as well as both molecular and alkali species[41]. Further, so far the demonstrated schemes for mid-circuit readout require an auxiliary laser to address specific atoms in the array. In our case, the single-site addressability only requires single tweezer depth control[42], which is a built-in feature of most tweezer platforms.

Motional Bell pairs and hyper-entanglement

Building upon the single qubit control showcased in the previous section, we now turn to generate entanglement between motional states of atoms in separate tweezers. We first demonstrate the preparation of motion-entangled Bell pairs, i.e. two atoms whose center-of-mass motion is entangled while their spin state is separable. Second, we demonstrate the simultaneous entanglement of multiple degrees of freedom per particle, known as hyper-entanglement[30,31]. Here, these multiple degrees of freedom are the electronic state of the atoms and their motion along a single axis.

We entangle the center-of-mass motion of two atoms by combining spin-motion conversion and spin-spin interactions mediated via excitation to high-lying Rydberg states (Fig. 4A). Starting with two atoms in $|0,\uparrow\rangle$, we first apply a spin $\pi/2$ pulse in order to prepare each in $|0,+\rangle$, for which we denote the two-atom state as $|00,++\rangle$. We then apply a controlled-Z gate through Rydberg interactions[12,14,16,41,58]. A final $\pi/4$ pulse rotates the state into the spin-entangled Bell state $|00,\Phi^+\rangle = \frac{1}{\sqrt{2}}|00\rangle \otimes (|\downarrow\downarrow\rangle + |\uparrow\uparrow\rangle)$. We then perform spin-motion transduction, obtaining a state which is spin-separable, but motion-entangled, $|\Phi^+,\uparrow\uparrow\rangle = \frac{1}{\sqrt{2}}(|00\rangle + |11\rangle) \otimes |\uparrow\uparrow\rangle$.

We characterize the resulting state by performing a parity measurement on the motional degree of freedom (Fig. 4B). This consists of evolution under the trapping

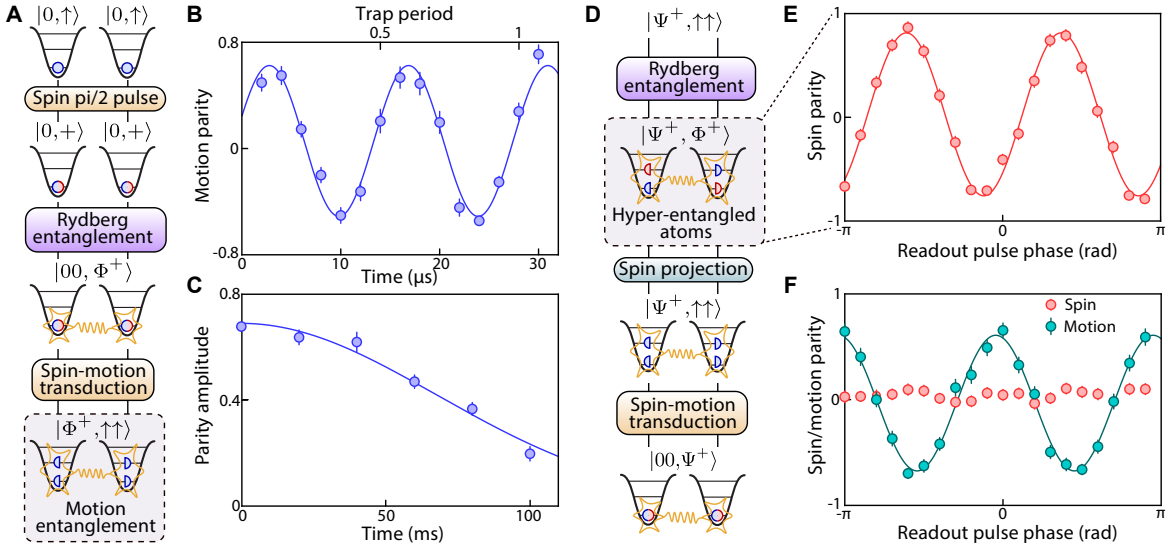

Fig. 4 | Entanglement and hyper-entanglement of motion and spin. A, Sketch of the protocol used to generate an entangled state of motion. After cooling the atoms and preparing the pseudo-spin superposition state $|0,+\rangle$, we entangle the spin degree of freedom via Rydberg interactions, preparing either the $|00,\Phi^+\rangle$ or the $|00,\Psi^+\rangle$ state[41] (see text). We then apply spin-motion transduction via sideband driving, transferring spin-entanglement to motion-entanglement, yielding $|\Phi^+,\uparrow\uparrow\rangle$, or $|\Psi^+,\uparrow\uparrow\rangle$. **B,** Parity oscillation measured by varying the time in $|\Phi^+,\uparrow\uparrow\rangle$ before converting back to pseudo-spin states for readout. The obtained oscillation frequency of $71.0^{+0.5}_{-0.5}$ kHz is consistent with twice the trap frequency $2\omega/(2\pi) \simeq 71$ kHz, as expected for $|\Phi^+,\uparrow\uparrow\rangle$. **C,** Motion parity amplitude as a function of time. We observe a Gaussian decay of fidelity with a typical $1/e$ decay time of 96^{+5}_{-5} ms. **D,** Sketch of the protocol used to generate hyper-entanglement of both spin and motion. We prepare the motion-entangled state $|\Psi^+,\uparrow\uparrow\rangle$, and apply a second entangling operation on the spin degree of freedom, producing the hyper-Bell state $|\Psi^+,\Phi^+\rangle$. In order to read out this hyper-entanglement, we project the spin component onto $|\Psi^+,\uparrow\uparrow\rangle$, then convert the motional entanglement into spin entanglement. **E,** Spin parity oscillation after hyper-entangling the atoms measured by applying a readout $\pi/2$-pulse and varying its phase. **F,** Parity oscillation after the spin projection, without (red) and with (green) spin-motion transduction. The parity oscillation collapses without spin-motion transduction, as the projection disentangles the spin part. However, the motion entanglement remains intact, which allows us to recover spin entanglement after performing the transduction.

potential for a variable amount of time, which induces a phase difference between different motional states, followed by spin-motion transduction for readout. We observe an oscillation frequency of $\omega/(2\pi) \simeq 71.0^{+0.5}_{-0.5}$ kHz, consistent with the expectation of twice the trap frequency (green markers).

We also generate the odd parity Bell state[12] $|\Psi^+,\uparrow\uparrow\rangle = \frac{1}{\sqrt{2}}(|01\rangle + |10\rangle) \otimes |\uparrow\uparrow\rangle$ by altering the spin-$\pi/4$ rotation to yield the spin entangled state $|00,\Psi^+\rangle = \frac{1}{\sqrt{2}}|00\rangle \otimes (|\downarrow\uparrow\rangle + |\uparrow\downarrow\rangle)$, followed by transduction to the motional state. In this case, we do not observe a parity oscillation, since the energy gap between $|01\rangle$ and $|10\rangle$ is given only by the small difference in trap frequency between the two traps[41].

Combining the contrast of the parity oscillation with the measured populations in the states $|00\rangle$ and $|11\rangle$, we obtain a motional Bell state fidelity for the state $|\Phi^+,\uparrow\uparrow\rangle$ of $F^{\text{motion}}_{\text{Bell}} = 0.75^{+1}_{-1}$ (uncorrected for SPAM errors). Currently, this value is limited by the bare Bell state generation fidelity in the electronic manifold[41] and the combined transduction fidelity for both atoms.

Importantly, the lifetime of motionally-entangled states is relatively long. We quantify this by measuring the amplitude of the parity oscillation signal as a function of hold time (Fig. 4C). We embed this measurement in a motion-echo sequence, as in the single atom case[41], to remove the effects of shot-to-shot trap variation. We observe a Gaussian decay, with a $1/e$ decay time of 96^{+5}_{-5} ms. This coherence time is similar to the one obtained for the single-atom motional superposition case, and we expect this also to improve through better trap intensity stabilization.

These results demonstrate Bell pair generation of motional states in separate traps spaced by distances much larger than the spatial extent of the atomic wavefunction; in our particular implementation, traps are separated by ≈ 3.3 μm, while the ground state wavefunction spread along the array axis is only ≈60 nm. To our knowledge, this is the first demonstration of motional Bell pair generation for neutral atoms in general, following earlier work with ions[59].

Using this versatile control we can go one step beyond pure motional entanglement, and demonstrate hyper-entanglement of motion and electronic state. In a hyper-entangled state, more than a single degree of freedom is in an entangled state, yielding a larger Hilbert space with various applications such as entanglement purification[31,33], hyper-parallel quantum computation[30], or superdense coding [34,35]. To date, such hyper-entangled states have only been realized utilizing

multiple degrees of freedom in the state of a photon[31].

To accomplish this task, we prepare the motion-entangled state $|\Psi^+,\uparrow\uparrow\rangle$, and then apply a second entangling operation on the electronic degree of freedom. As opposed to hyperfine or nuclear qubits, the Rydberg drive couples nearly identically to both levels of the motional qubit, up to a detuning $\delta \simeq 2\pi \times 35\,\mathrm{kHz}$ that is much smaller than the Rabi frequency $\Omega \simeq 2\pi \times 3.5\,\mathrm{MHz}$ applied. The gate thus acts on the electronic degree of freedom, leaving the motional state largely unchanged, generating the hyper-Bell state $|\Psi^+,\Phi^+\rangle$.

To show that entanglement coexists on the two degrees of freedom, we first measure the spin parity and population (Fig. 4E). We obtain an entanglement fidelity $F_{\mathrm{Bell}}^{\mathrm{spin}} = 0.855^{+7}_{-7}$. To show the simultaneous motional entanglement, we perform our fast imaging procedure[40] to project the $|\Psi^+,\Phi^+\rangle$ state onto $|\Psi^+,\uparrow\uparrow\rangle$ or $|\Psi^+,\downarrow\downarrow\rangle$ with equal probability. Atoms in $|\downarrow\rangle$ have a low probability of surviving the fast imaging[40], so in the following we only consider pairs projected into $|\Psi^+,\uparrow\uparrow\rangle$.

We first verify that no spin entanglement remains by measuring a null spin parity (Fig. 4F, red markers). We then apply spin-motion transduction, and again recover a parity oscillation signal (green markers), indicating that the motion-entanglement was preserved. We obtain $F_{\mathrm{Bell}}^{\mathrm{motion}} = 0.76^{+1}_{-1}$. Even with the complications of the hyper-entanglement sequence, this value is comparable to the one obtained using the sequence described in Fig. 4A, indicating that Rydberg entanglement and spin projection do not appreciably affect motion-entanglement.

Conclusion and outlook

In this work, we have demonstrated how controlling motion in tweezers can be used to perform quantum information processing tasks. Such control is enabled by a novel cooling mechanism based on the detection and correction of motional excitations. This technique can be applied to any tweezer platform, including those trapping alkali or molecular species[41], and should also be applicable to ion-based platforms[37], as well as neutral atoms trapped in optical lattices. We find that this new mechanism systematically outperforms even idealized sideband cooling, which we experimentally demonstrated in realistic scenarios.

We then showed the coherent manipulation of motional states, and how these can be used to perform mid-circuit readout of an optical qubit without utilizing ancillary nuclear states. Importantly, this optical qubit is used by the currently most precise optical atomic clocks[53,60–62], the performance of which could be enhanced via multi-ensemble metrology[42,57,63] using mid-circuit measurement.

Finally, we demonstrated motional entanglement of two tweezer-trapped atoms while leaving their electronic degrees of freedom separable, which we then extended to simultaneous hyper-entanglement of both motion and electronic states. To our knowledge, this is the first such demonstration of hyper-entanglement in any matter-based platform. Our scheme is naturally extensible to control over all three motional axes, allowing up to four Bell states worth of entanglement (one electronic, three motional) to be stored in a single pair of atoms. Given the long-lived nature of the motional entanglement, one could perform quantum computation tasks in the spin degree of freedom, and quantum memory tasks on the motional degree of freedom, and for example perform hyper-parallel quantum computation[30,31], entanglement purification[31,33], superdense coding[34,35], or measure non-trivial quantities such as Rényi entropy or fidelity overlaps via two-copy interference protocols[36].

This work paves the way for realizing quantum information processing tasks utilizing these motional states. A natural extension of our work is to use the full bosonic degree of freedom to implement quantum error correction schemes[26,27], or to study lattice gauge theories[28,29]. Furthermore, the mid-circuit readout and motion entanglement described here could be combined to perform ancilla-based detection and quantum error correction codes[1,2,64]. Finally, the controlled entanglement of the motion of atoms separated at mesoscopic distances could lead to entanglement-enhanced tests of short-length gravitational effects[65].

ACKNOWLEDGMENTS

We acknowledge insightful discussions with, and comments from, Harry Levine, Johannes Zeiher, Daniel Barredo, Arian Jadbabaie, and Xiangkai Sun. We acknowledge support from the Army Research Office MURI program (W911NF2010136), the NSF QLCI program (2016245), the Institute for Quantum Information and Matter, an NSF Physics Frontiers Center (NSF Grant PHY-1733907), the DARPA ONISQ program (W911NF2010021), the U.S. Department of Energy, Office of Science, National Quantum Information Science Research Centers, Quantum Systems Accelerator, and the NSF CAREER award (1753386). PS acknowledges support from the IQIM postdoctoral fellowship. RF acknowledges support from the Troesh postdoctoral fellowship. RBST acknowledges support from the Taiwan-Caltech Fellowship.

[1] P. W. Shor, Scheme for reducing decoherence in quantum computer memory, Phys. Rev. A **52**, R2493 (1995).
[2] E. Knill, R. Laflamme, and W. Zurek, Threshold accuracy for quantum computation, arXiv:quant-ph/9610011 (1996).
[3] G. Tóth and I. Apellaniz, Quantum metrology from

a quantum information science perspective, Journal of Physics A: Mathematical and Theoretical **47**, 424006 (2014).
[4] S. Wehner, D. Elkouss, and R. Hanson, Quantum internet: A vision for the road ahead, Science **362**, eaam9288 (2018).
[5] F. Xu, X. Ma, Q. Zhang, H.-K. Lo, and J.-W. Pan, Secure quantum key distribution with realistic devices, Reviews of Modern Physics **92**, 025002 (2020).
[6] G. Wendin, Quantum information processing with superconducting circuits: a review, Reports on Progress in Physics **80**, 106001 (2017).
[7] C. D. Bruzewicz, J. Chiaverini, R. McConnell, and J. M. Sage, Trapped-ion quantum computing: Progress and challenges, Applied Physics Reviews **6**, 021314 (2019).
[8] S. Slussarenko and G. J. Pryde, Photonic quantum information processing: A concise review, Applied Physics Reviews **6**, 041303 (2019).
[9] P. K. Shandilya, S. Flågan, N. C. Carvalho, E. Zohari, V. K. Kavatamane, J. E. Losby, and P. E. Barclay, Diamond integrated quantum nanophotonics: Spins, photons and phonons, Journal of Lightwave Technology **40**, 7538 (2022).
[10] M. Kang, W. C. Campbell, and K. R. Brown, Quantum error correction with metastable states of trapped ions using erasure conversion, PRX Quantum **4**, 020358 (2023).
[11] M. Saffman, Quantum computing with atomic qubits and Rydberg interactions: progress and challenges, Journal of Physics B: Atomic, Molecular and Optical Physics **49**, 202001 (2016).
[12] H. Levine, A. Keesling, G. Semeghini, A. Omran, T. T. Wang, S. Ebadi, H. Bernien, M. Greiner, V. Vuletić, H. Pichler, et al., Parallel implementation of high-fidelity multiqubit gates with neutral atoms, Physical Review Letters **123**, 170503 (2019).
[13] A. Browaeys and T. Lahaye, Many-body physics with individually controlled Rydberg atoms, Nature Physics **16**, 132 (2020).
[14] S. Ma, G. Liu, P. Peng, B. Zhang, S. Jandura, J. Claes, A. P. Burgers, G. Pupillo, S. Puri, and J. D. Thompson, High-fidelity gates and mid-circuit erasure conversion in an atomic qubit, Nature **622**, 279 (2023).
[15] S. de Léséleuc, D. Barredo, V. Lienhard, A. Browaeys, and T. Lahaye, Analysis of imperfections in the coherent optical excitation of single atoms to Rydberg states, Physical Review A **97**, 53803 (2018).
[16] N. Schine, A. W. Young, W. J. Eckner, M. J. Martin, and A. M. Kaufman, Long-lived bell states in an array of optical clock qubits, Nature Physics **18**, 1067 (2022).
[17] D. Bluvstein, H. Levine, G. Semeghini, T. T. Wang, S. Ebadi, M. Kalinowski, A. Keesling, N. Maskara, H. Pichler, M. Greiner, et al., A quantum processor based on coherent transport of entangled atom arrays, Nature **604**, 451 (2022).
[18] A. L. Shaw, R. Finkelstein, R. B.-S. Tsai, P. Scholl, T. H. Yoon, J. Choi, and M. Endres, Multi-ensemble metrology by programming local rotations with atom movements, arXiv:2303.16885 (2023).
[19] M. O. Brown, S. R. Muleady, W. J. Dworschack, R. J. Lewis-Swan, A. M. Rey, O. Romero-Isart, and C. A. Regal, Time-of-flight quantum tomography of an atom in an optical tweezer, Nature Physics **19**, 569 (2023).
[20] T. Hartke, B. Oreg, N. Jia, and M. Zwierlein, Quantum register of fermion pairs, Nature **601**, 537 (2022).
[21] P. L. Knight, E. A. Hinds, M. B. Plenio, D. J. Wineland, M. Barrett, J. Britton, J. Chiaverini, B. DeMarco, W. M. Itano, B. Jelenković, et al., Quantum information processing with trapped ions, Philosophical Transactions of the Royal Society of London. Series A: Mathematical, Physical and Engineering Sciences **361**, 1349 (2003).
[22] C. Flühmann, T. L. Nguyen, M. Marinelli, V. Negnevitsky, K. Mehta, and J. P. Home, Encoding a qubit in a trapped-ion mechanical oscillator, Nature **566**, 513 (2019).
[23] R. W. Heeres, P. Reinhold, N. Ofek, L. Frunzio, L. Jiang, M. H. Devoret, and R. J. Schoelkopf, Implementing a universal gate set on a logical qubit encoded in an oscillator, Nature Communications **8**, 94 (2017).
[24] P. Campagne-Ibarcq, A. Eickbusch, S. Touzard, E. Zalys-Geller, N. E. Frattini, V. V. Sivak, P. Reinhold, S. Puri, S. Shankar, R. J. Schoelkopf, et al., Quantum error correction of a qubit encoded in grid states of an oscillator, Nature **584**, 368 (2020).
[25] K. Singh, C. E. Bradley, S. Anand, V. Ramesh, R. White, and H. Bernien, Mid-circuit correction of correlated phase errors using an array of spectator qubits, Science **380**, 1265 (2023).
[26] D. Gottesman, A. Kitaev, and J. Preskill, Encoding a qubit in an oscillator, Phys. Rev. A **64**, 012310 (2001).
[27] C. Flühmann, T. L. Nguyen, M. Marinelli, V. Negnevitsky, K. Mehta, and J. P. Home, Encoding a qubit in a trapped-ion mechanical oscillator, Nature **566**, 513 (2019).
[28] S. P. Jordan, K. S. M. Lee, and J. Preskill, Quantum computation of scattering in scalar quantum field theories, Quantum Info. Comput. **14**, 1014–1080 (2014).
[29] A. Macridin, A. C. Y. Li, S. Mrenna, and P. Spentzouris, Bosonic field digitization for quantum computers, Phys. Rev. A **105**, 052405 (2022).
[30] B.-C. Ren and F.-G. Deng, Hyper-parallel photonic quantum computation with coupled quantum dots, Scientific Reports **4**, 4623 (2014).
[31] F.-G. Deng, B.-C. Ren, and X.-H. Li, Quantum hyperentanglement and its applications in quantum information processing, Science Bulletin **62**, 46 (2017).
[32] X.-F. Shi, Hyperentanglement of divalent neutral atoms by rydberg blockade, Phys. Rev. A **104**, 042422 (2021).
[33] X.-M. Hu, C.-X. Huang, Y.-B. Sheng, L. Zhou, B.-H. Liu, Y. Guo, C. Zhang, W.-B. Xing, Y.-F. Huang, C.-F. Li, et al., Long-distance entanglement purification for quantum communication, Phys. Rev. Lett. **126**, 010503 (2021).
[34] X.-M. Hu, Y. Guo, B.-H. Liu, Y.-F. Huang, C.-F. Li, and G.-C. Guo, Beating the channel capacity limit for superdense coding with entangled ququarts, Science Advances **4**, eaat9304 (2018).
[35] T. M. Graham, H. J. Bernstein, T. C. Wei, M. Junge, and P. G. Kwiat, Superdense teleportation using hyperentangled photons, Nature Communications 2015 6:1 **6**, 1 (2015).
[36] H. Pichler, G. Zhu, A. Seif, P. Zoller, and M. Hafezi, Measurement protocol for the entanglement spectrum of cold atoms, Phys. Rev. X **6**, 041033 (2016).
[37] C. Lee, S. C. Webster, J. Mosca Toba, O. Corfield, G. Porter, and R. C. Thompson, Measurement-based ground-state cooling of a trapped-ion oscillator, Phys.

Rev. A **107**, 033107 (2023).
[38] M. Grassl, T. Beth, and T. Pellizzari, Codes for the quantum erasure channel, Phys. Rev. A **56**, 33 (1997).
[39] Y. Wu, S. Kolkowitz, S. Puri, and J. D. Thompson, Erasure conversion for fault-tolerant quantum computing in alkaline earth Rydberg atom arrays, Nature Communications **13**, 4657 (2022).
[40] P. Scholl, A. L. Shaw, R. B.-S. Tsai, R. Finkelstein, J. Choi, and M. Endres, Erasure conversion in a high-fidelity Rydberg quantum simulator, Nature **622**, 273 (2023).
[41] See supplemental material.
[42] A. L. Shaw, P. Scholl, R. Finklestein, I. S. Madjarov, B. Grinkemeyer, and M. Endres, Dark-state enhanced loading of an optical tweezer array, Phys. Rev. Lett. **130**, 193402 (2023).
[43] E. Deist, Y.-H. Lu, J. Ho, M. K. Pasha, J. Zeiher, Z. Yan, and D. M. Stamper-Kurn, Mid-circuit cavity measurement in a neutral atom array, Phys. Rev. Lett. **129**, 203602 (2022).
[44] T. M. Graham, L. Phuttitarn, R. Chinnarasu, Y. Song, C. Poole, K. Jooya, J. Scott, A. Scott, P. Eichler, and M. Saffman, Mid-circuit measurements on a neutral atom quantum processor, arXiv:2303.10051 (2023).
[45] J. W. Lis, A. Senoo, W. F. McGrew, F. Rönchen, A. Jenkins, and A. M. Kaufman, Mid-circuit operations using the omg-architecture in neutral atom arrays, arXiv:2305.19266 (2023).
[46] M. A. Norcia, W. B. Cairncross, K. Barnes, P. Battaglino, A. Brown, M. O. Brown, K. Cassella, C. A. Chen, R. Coxe, D. Crow, et al., Mid-circuit qubit measurement and rearrangement in a ^{171}Yb atomic array, arXiv:2305.19119 (2023).
[47] I. S. Madjarov, J. P. Covey, A. L. Shaw, J. Choi, A. Kale, A. Cooper, H. Pichler, V. Schkolnik, J. R. Williams, and M. Endres, High-fidelity entanglement and detection of alkaline-earth Rydberg atoms, Nature Physics **16**, 857 (2020).
[48] A. Cooper, J. P. Covey, I. S. Madjarov, S. G. Porsev, M. S. Safronova, and M. Endres, Alkaline-earth atoms in optical tweezers, Physical Review X **8**, 41055 (2018).
[49] M. A. Norcia, A. W. Young, and A. M. Kaufman, Microscopic control and detection of ultracold strontium in optical-tweezer arrays, Physical Review X **8**, 41054 (2018).
[50] M. Endres, H. Bernien, A. Keesling, H. Levine, E. R. Anschuetz, A. Krajenbrink, C. Senko, V. Vuletic, M. Greiner, and M. D. Lukin, Atom-by-atom assembly of defect-free one-dimensional cold atom arrays, Science **354**, 1024 (2016).
[51] D. Barredo, S. de Leseleuc, V. Lienhard, T. Lahaye, and A. Browaeys, An atom-by-atom assembler of defect-free arbitrary two-dimensional atomic arrays, Science **354**, 1021 (2016).
[52] X. Zhang, K. Beloy, Y. S. Hassan, W. F. McGrew, C.-C. Chen, J. L. Siegel, T. Grogan, and A. D. Ludlow, Subrecoil clock-transition laser cooling enabling shallow optical lattice clocks, Phys. Rev. Lett. **129**, 113202 (2022).
[53] I. S. Madjarov, A. Cooper, A. L. Shaw, J. P. Covey, V. Schkolnik, T. H. Yoon, J. R. Williams, and M. Endres, An atomic-array optical clock with single-atom readout, Physical Review X **9**, 41052 (2019).
[54] B. M. Terhal, Quantum error correction for quantum memories, Rev. Mod. Phys. **87**, 307 (2015).
[55] J. Y. Lee, W. Ji, Z. Bi, and M. P. A. Fisher, Decoding measurement-prepared quantum phases and transitions: from Ising model to gauge theory, and beyond, arXiv:2208.11699 (2022).
[56] R. Verresen, N. Tantivasadakarn, and A. Vishwanath, Efficiently preparing Schrödinger's cat, fractons and non-abelian topological order in quantum devices, arXiv:2112.03061 (2022).
[57] T. Rosenband and D. R. Leibrandt, Exponential scaling of clock stability with atom number (2013).
[58] S. J. Evered, D. Bluvstein, M. Kalinowski, S. Ebadi, T. Manovitz, H. Zhou, S. H. Li, A. A. Geim, T. T. Wang, N. Maskara, et al., High-fidelity parallel entangling gates on a neutral-atom quantum computer, Nature **622**, 268 (2023).
[59] J. D. Jost, J. P. Home, J. M. Amini, D. Hanneke, R. Ozeri, C. Langer, J. J. Bollinger, D. Leibfried, and D. J. Wineland, Entangled mechanical oscillators, Nature **459**, 683 (2009).
[60] M. A. Norcia, A. W. Young, W. J. Eckner, E. Oelker, J. Ye, and A. M. Kaufman, Seconds-scale coherence on an optical clock transition in a tweezer array, Science **366**, 93 (2019).
[61] A. W. Young, W. J. Eckner, W. R. Milner, D. Kedar, M. A. Norcia, E. Oelker, N. Schine, J. Ye, and A. M. Kaufman, Half-minute-scale atomic coherence and high relative stability in a tweezer clock, Nature **588**, 408 (2020).
[62] T. Bothwell, C. J. Kennedy, A. Aeppli, D. Kedar, J. M. Robinson, E. Oelker, A. Staron, and J. Ye, Resolving the gravitational redshift across a millimetre-scale atomic sample, Nature **602**, 420 (2022).
[63] X. Zheng, J. Dolde, and S. Kolkowitz, Reducing the instability of an optical lattice clock using multiple atomic ensembles, arXiv:2305.12315 (2023).
[64] C. K. Andersen, A. Remm, S. Lazar, S. Krinner, J. Heinsoo, J.-C. Besse, M. Gabureac, A. Wallraff, and C. Eichler, Entanglement stabilization using ancilla-based parity detection and real-time feedback in superconducting circuits, npj Quantum Information **5**, 69 (2019).
[65] G. M. Tino, Testing gravity with cold atom interferometry: results and prospects, Quantum Science and Technology **6**, 024014 (2021).
[66] J. P. Covey, I. S. Madjarov, A. Cooper, and M. Endres, 2000-times repeated imaging of strontium atoms in clock-magic tweezer arrays, Physical Review Letters **122**, 173201 (2019).
[67] C. Weitenberg, M. Endres, J. F. Sherson, M. Cheneau, P. Schauß, T. Fukuhara, I. Bloch, and S. Kuhr, Single-spin addressing in an atomic mott insulator, Nature **471**, 319 (2011).
[68] S. Dörscher, R. Schwarz, A. Al-Masoudi, S. Falke, U. Sterr, and C. Lisdat, Lattice-induced photon scattering in an optical lattice clock, Phys. Rev. A **97**, 063419 (2018).
[69] S. Jandura and G. Pupillo, Time-Optimal Two- and Three-Qubit Gates for Rydberg Atoms, Quantum **6**, 712 (2022).
[70] A. Pagano, S. Weber, D. Jaschke, T. Pfau, F. Meinert, S. Montangero, and H. P. Büchler, Error budgeting for a controlled-phase gate with strontium-88 Rydberg atoms, Phys. Rev. Res. **4**, 033019 (2022).
[71] J. Choi, A. L. Shaw, I. S. Madjarov, X. Xie, R. Finkelstein, J. P. Covey, J. S. Cotler, D. K. Mark, H.-Y. Huang,

A. Kale, et al., Preparing random states and benchmarking with many-body quantum chaos, Nature **613**, 468 (2023).

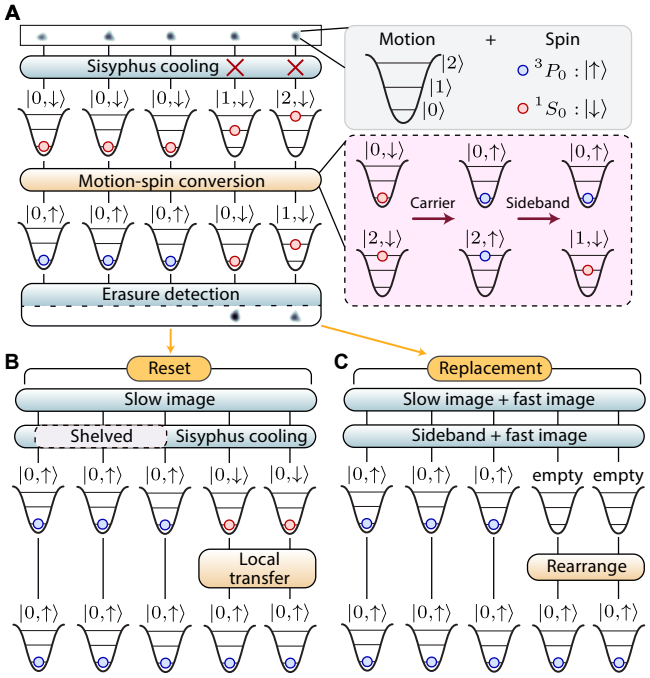

Fig. S1 | Details on the erasure cooling mechanism. **A,** After cooling the atoms using Sisyphus cooling, we transfer the atoms in $|\downarrow\rangle$ to the $|\uparrow\rangle$ state using a carrier pulse, which conserves the motional state of the atoms. We then apply a blue sideband pulse, which performs the $|n,\uparrow\rangle \rightarrow |n-1,\downarrow\rangle$ transition, where n is the atom's motional level. We then selectively image atoms in $|\downarrow\rangle$. **B,** In the reset case, the erasure detection image is a slow and non-destructive image. After the image, we cool the atoms again. Atoms in $|0,\uparrow\rangle$ are shelved from the Sisyphus cooling mechanism. We then selectively transfer[18] the atoms which were imaged in $|\downarrow\rangle$ to $|\uparrow\rangle$. **C,** For the replacement method, the erasure detection image is a combination of a slow, high survival image, and a fast, low survival image. We then repeat a sideband pulse and a fast image in order to improve the erasure cooling efficiency. We then fill the emptied tweezers with auxiliary atoms which were measured to be in the $|0,\uparrow\rangle$ state.

MATERIAL AND METHODS

Details on erasure cooling

Here we detail the erasure correction cooling (ECC) mechanism. We start with the erasure detection of motional excitations, then describe the two methods employed to perform error correction.

The erasure detection is described in Fig. S1A. After cooling the atoms with Sisyphus cooling using the $^3P_1$ level, we transfer the atoms in $|\downarrow\rangle$ to the $|\uparrow\rangle$ state using a carrier pulse, which conserves the motional state of the atoms. We then apply a blue sideband pulse which performs the $|n,\uparrow\rangle \rightarrow |n-1,\downarrow\rangle$ transition, where n is the atom's motional level. Atoms in $|0,\uparrow\rangle$ are not transferred back to $|\downarrow\rangle$. We then selectively image atoms in $|\downarrow\rangle$, which allows us to spatially resolve the position of motional excitations in the array. We then correct for

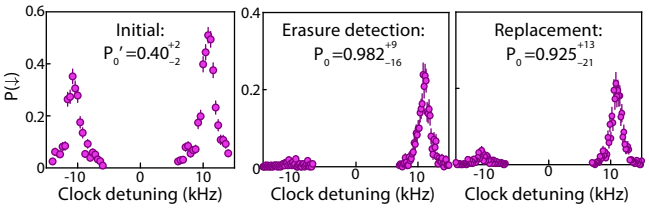

Fig. S2 | Erasure correction cooling in the axial direction. Probability P_0 for an atom to be in the $|0\rangle$ state measured via sideband spectroscopy, in the axial direction of the tweezers. We show the results without erasure correction cooling, performing erasure conversion with post-selection (not correction), and with correction using the replacement method.

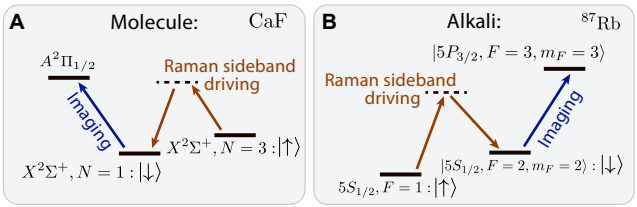

Fig. S3 | Erasure correction cooling in other platforms. A, Good candidates in molecules, using the example of calcium-fluoride. **B,** Good candidates in alkalis, using the example of rubidium.

these errors using two methods: re-using the same atoms by selectively cooling them again (reset) or replacing them with auxiliary atoms in the $|0,\uparrow\rangle$ state (replacement).

We first detail the reset method (see Fig. S1B). In this case, the erasure detection is a slow, high survival image with a duration of 45 ms[66]. After the image, we cool the atoms in $|\downarrow\rangle$ again through Sisyphus cooling, while atoms in $|0,\uparrow\rangle$ are shelved from this cooling. We then use movement-induced phase shifts to selectively transfer[18] to $|\uparrow\rangle$ the atoms which were previously imaged in $|\downarrow\rangle$. This process can be repeated several times in order to improve the erasure cooling efficiency.

The erasure detection image in the case of the replacement method (see Fig. S1C) is a combination of a high survival, slow image[66] with a duration of 30 ms and a fast, low survival[40] image with a duration of 24 μs. We perform this combination in order to maximize the imaging fidelity while minimizing the misidentification of Raman scattering events from the $|\uparrow\rangle$ state to the $|\downarrow\rangle$ state. We then perform another blue sideband pulse and a fast image in order to minimize the effect of tweezer-induced heating during the erasure detection, which improves the eventual erasure cooling efficiency. Due to the fast image, the tweezers holding atoms in $|\downarrow\rangle$ are empty. We fill them with auxiliary atoms which were measured to be in the $|0,\uparrow\rangle$ state.

We ramp down the tweezers depth to $\sim 40\,\mu$K, which corresponds to one-tenth of their nominal depth in order to reduce the effect of tweezer-induced heating such as Rayleigh scattering. In particular, we also observe that rearrangement-induced heating strongly depends on tweezers depth, and is minimized for tweezers depth in the range $\sim 20 - 40\,\mu$K. This rearrangement-induced heating is identified to be coming from (i) the finite probability that an atom is heated during transportation, and (ii) tweezers depth oscillations during atom movement due to intermodulation of the varying frequencies in the acousto-optic deflector used to generate the tweezers[50], although we leave a quantitative analysis of these effects to future work.

Erasure cooling in the axial direction

The erasure cooling results presented in the main text concern one of the tightly-confining radial direction. We here show that the method also applies to the axial direction, enabling this new cooling mechanism to be used to perform 3D cooling in principle. The overall method is the same as described earlier, and the only difference lies in the direction of the sideband driving beam with respect to the tweezer axis. We use a beam that propagates in the same direction as the tweezer, allowing us to drive sideband transitions on the axial direction of the tweezers, for which the trapping frequency is $2\pi \times 10.7\,$kHz. The results are shown in Fig S2. We start with a motional ground state population $P_0' = 0.40^{+2}_{-2}$ after Sisyphus cooling, which is lower than the radial direction due to the lower trapping frequency. Applying erasure correction cooling, we obtain $P_0 = 0.982^{+9}_{-18}$ after erasure detection and post-selection, and $P_0 = 0.925^{+13}_{-25}$ with active correction using the replacement method. These results are also better than what can be achieved using sideband cooling on the $^3P_1$ transition for this trapping frequency (see Fig. 3E), showing a practical advantage in using erasure correction cooling over sideband cooling.

Erasure correction cooling on other platforms

We here show that ECC is, in principle, applicable to any tweezer platform, and detail which states can be used for the $|\downarrow\rangle$ and $|\uparrow\rangle$ when implementing ECC. Our present work uses strontium, and a generalization to other alkaline-earth(-like) atoms is trivial, so we focus on platforms using molecules and alkalis (Fig. S3).

As discussed in the main text, the two key ingredients to implement ECC are (i) driving sideband transitions between $|\downarrow\rangle$ and $|\uparrow\rangle$, and (ii) the ability to selectively detect $|\downarrow\rangle$ while $|\uparrow\rangle$ is shelved. These ingredients are present in both molecules and alkalis.

For molecules (Fig. S3A), good candidates are two different rotational states, such as $|\downarrow\rangle = X^2\Sigma^+, N = 1$ and $|\uparrow\rangle = X^2\Sigma^+, N = 3$ in calcium fluoride. Sideband transitions can be achieved through Raman processes, and selective imaging of $|\downarrow\rangle$ is achieved through driving the closed-transition to $A^2\Pi_{1/2}$, for which $|\uparrow\rangle$ is shelved.

For alkalis (Fig. S3B), good candidates are two different hyperfine states, such as $|\downarrow\rangle = |5S_{1/2}, F = 2, m_F = 2\rangle$ and $|\uparrow\rangle = |5S_{1/2}, F = 1, m_F = 1\rangle$ in rubidium 87. Sideband transitions can be achieved through a Raman process, and selective imaging of $|\downarrow\rangle$ is achieved through driving the closed-transition to $|5P_{3/2}, F = 3, m_F = 3\rangle$, for which $|\uparrow\rangle$ is shelved.

In principle ECC is also applicable to ion-based platforms, for which post-selection on detected erasures has been recently reported[37]. Furthermore, ECC should also work for neutral atoms and molecules trapped in optical lattices by using the reset method combined with local addressing in order to perform the local rotations[67].

Cooling simulations

Here we provide details on the cooling simulations results presented in Fig. 2E. We first describe sideband cooling on the $^3P_1$ level of strontium, then the idealized sideband cooling, and finally both idealized and noisy erasure cooling using replacement.

In all cases, we simulate the following one-dimensional Hamiltonian

$$H = \hbar\omega(a^\dagger a + \frac{1}{2}) - \hbar\Delta|\uparrow\rangle\langle\uparrow| + \frac{1}{2}\hbar\Omega(e^{i\eta(a+a^\dagger)}|\uparrow\rangle\langle\downarrow| + \text{h.c.}), \tag{S1}$$

where $a^\dagger$ (a) is the creation (annihilation) operator acting on the motional levels, ω is the trapping frequency, Δ is the detuning, η is the Lamb-Dicke factor and Ω is the Rabi frequency. We set $\Delta = -\omega$, and use a basis of ten motional states.

Ideal sideband cooling on $^3P_1$

We perform a simulation of sideband cooling on the $|^3P_1, m_J = 0\rangle$ state. Here we assume ideal conditions, namely: (i) we assume no laser noise, (ii) we set a Rabi frequency 500 times smaller than the cooling state linewidth, and (iii) we consider cooling only in a single direction, but take into account the dipole radiation pattern in 3D (more details below).

We solve the Master equation in which we take into account spontaneous emission from the $|\uparrow\rangle$ state and its associated momentum kick which follows a dipole pattern distribution:

$$i\hbar\partial_t\rho = (H_\Gamma\rho - \rho H_\Gamma^\dagger) + i\hbar\Gamma\int d\theta D(\theta) c_\theta \rho c_\theta^\dagger.$$

We define $H_\Gamma = H - \frac{i}{2}\hbar\Gamma|\uparrow\rangle\langle\uparrow|$, and $c_\theta = e^{-i|k|\cos(\theta)}|\downarrow\rangle\langle\uparrow|$. Here, ρ is the density matrix of the spin and motional states, $\Gamma = 2\pi \times 7.4\,\text{kHz}$ is the linewidth of $^3P_1$, $D(\theta) = 3\sin^2(\theta)/(8\pi)$ is the dipole radiation pattern for the transition of interest, θ the angle of emission with respect to the quantization axis. The dipole emission pattern takes this simple form thanks to considering cooling on the $|^3P_1, m_J = 0\rangle$ state.

We use as an initial condition a thermal distribution of motional states with mean vibrational level $\bar{n} = 1$. We set $\Omega = \Gamma/500$, and perform the simulation for 1000 Rabi cycles. This ensures that we reach the system's steady state, and that the effect of the finite Ω on the final motional state populations is negligible.

We note that in this work, we do not perform a simulation of cooling in the three directions of space, even though we take into account the dipole emission pattern in 3D. We assume that there is no thermalization between the different axes; if such cross-axis thermalization did exist it would lead to a higher temperature than we find here.

Idealized sideband cooling

We consider sideband cooling on an idealized cooling transition, which is defined as having an infinitely narrow linewidth ($\Gamma = 0$), but still having the ability to decay to the spin ground state. We set $\Omega = 2\pi \times 2.5\,\text{kHz}$ and assume that the difference in energy between the spin states is given by a wavelength of 698 nm, which would correspond to cooling on the $^3P_0$ state of strontium. We initialize the system in a thermal distribution with $\bar{n} = 1$, and perform the following simulation. We evolve the system's state for a duration corresponding to a sideband π pulse. We then project the state onto $|\downarrow\rangle$ in order to mimic spontaneous decay. During this event, a momentum kick is provided to the atom following the radiation dipole pattern described earlier. We repeat this process 100 times, which ensures that we reach the system's steady state.

Idealized erasure correction cooling using replacement

The idealized erasure correction cooling simulations are similar to the idealized sideband cooling. We set $\Omega = 2\pi \times 2.5\,\text{kHz}$ and initialize the system in a thermal distribution with $\bar{n} = 1$. We then perform the following simulation. Starting in $|\uparrow\rangle$, we evolve the system's state for a duration corresponding to a sideband π pulse. In order to simulate a perfect erasure detection and replacement, we get rid of the population in $|\downarrow\rangle$, and renormalize the population of the various motional levels in $|\uparrow\rangle$. We repeat this process 100 times, which ensures that we reach the system's steady state.

Noisy simulation of erasure correction cooling using replacement

We finally describe the simulation of erasure correction cooling using replacement including relevant imperfections. We solve the Master equation described earlier

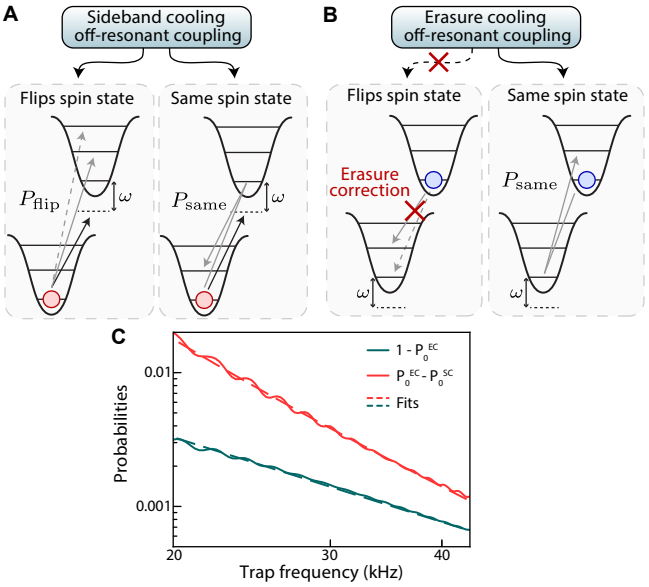

Fig. S4 | Limits of sideband cooling and erasure correction cooling A, The limit in sideband cooling efficiency is due to the off-resonant coupling to motional levels which are not the ground state ($n > 0$), either (i) in the opposite pseudo-spin state as the initial one $|n, \uparrow\rangle$, or (ii) in the same spin state $|n, \downarrow\rangle$ via an off-resonant two-photon process. **B,** In the case of erasure correction cooling, off-resonant coupling to the opposite spin state $|n, \downarrow\rangle$ is detected and hence does not contribute to the finite efficiency. The limit is the off-resonant two-photon transition to $|n, \uparrow\rangle$. **C,** Simulated efficiency of ideal ECC $1 - P_0^{\text{EC}}$ (red line), and difference between sideband cooling and ECC efficiencies $P_0^{\text{EC}} - P_0^{\text{SC}}$ (green line), as a function of trap frequency ω. We fit the data using $f(\omega) = A(1/\omega)^B$, with A and B as free parameters (dashed lines). The obtained exponents are $B = 1.9^{+1}_{-1}$ for $1 - P_0^{\text{EC}}$ and $B = 2.9^{+1}_{-1}$ for $P_0^{\text{EC}} - P_0^{\text{SC}}$, which is consistent with our expectations.

in which we take into account the finite lifetime of the $^3P_0$ state, and the tweezer-induced heating rate, which we implement by adding a jump operator acting on the motional states; the tweezer-induced heating is independently measured as an increase in mean vibrational number by 3.0(4) s^{-1}. We initialize the system in a thermal distribution with $P_0' = 0.77$, and simulate the sequence described in Fig. S1. We assume a perfect imaging fidelity in the erasure detection but take into account the tweezer-induced heating during the imaging and replacement times.

Fundamental limits of sideband cooling and erasure correction cooling

In the main text, we experimentally show that erasure correction cooling (ECC) using the replacement method leads to higher P_0 than a simulation of idealized sideband cooling (SC), for a specific range of parameters. Here we explain why, on a fundamental level, this new cooling mechanism leads to a larger P_0 than SC for any trapping frequency. We further determine the scaling of the ECC efficiency in the sideband resolved and Lamb-Dicke regimes, as a function of the trap frequency.

Fundamental limits

We start by describing the fundamental limits of sideband cooling. We assume that the atoms are initialized in $|0, \downarrow\rangle$, and that we drive a red sideband transition in order to cool the atoms. In this situation, sideband cooling has a finite probability to actually heat the atoms via off-resonant couplings to any motional state $|n, \uparrow\rangle$. Note that in the deep Lamb-Dicke regime, spontaneous emission does not lead to a change in motional state, and thus off-resonant coupling to $|0, \downarrow\rangle$ does not impact the finite cooling efficiency.

These off-resonant couplings affect the system in two qualitatively different ways (Fig. S4A): (i) the off-resonant coupling flips the initial pseudo-spin state to reach $|n, \uparrow\rangle$ with probability P_{flip}, and (ii) an off-resonant two-photon process which transfers the atoms in $|n, \downarrow\rangle$ and $n > 0$, with probability P_{same}. The values of P_{flip} and P_{same} depend on the Rabi frequency, Lamb-Dicke factor, and trap frequency, and are detailed below. The eventual fundamental limit in SC is therefore the sum of these two contributions:

$$P_0^{\text{SC}} = 1 - P_{\text{flip}} - P_{\text{same}},$$

where P_0^{SC} is the fundamental limit of the $|0\rangle$ population with sideband cooling.

We now turn to the case of ECC, and consider off-resonant coupling out of the initial state $|0, \uparrow\rangle$ (see Fig. S4B). For ECC, off-resonant coupling to opposite spin states $|n, \downarrow\rangle$ does not impact the ECC cooling efficiency: any atom transferred to $|\downarrow\rangle$ is detected and replaced, which can be effectively seen as $P_{\text{flip}} = 0$. The fundamental limit is thus given only by the pseudo-spin conserving, off-resonant two-photon transition $|0, \uparrow\rangle \rightarrow |n, \uparrow\rangle$, which cannot be converted into an erasure in our scheme. We therefore get:

$$P_0^{\text{EC}} = 1 - P_{\text{same}},$$

where P_0^{EC} is the fundamental limit in $|0\rangle$ population with erasure correction cooling.

We note that the value of P_{same} is the same in both cooling methods, as the action employed to cool the atoms – a red sideband pulse – is exactly the same for both methods. We therefore obtain that

$$P_0^{\text{EC}} - P_0^{\text{SC}} = P_{\text{flip}},$$

meaning that P_0^{EC} is an upper bound for P_0^{SC}.

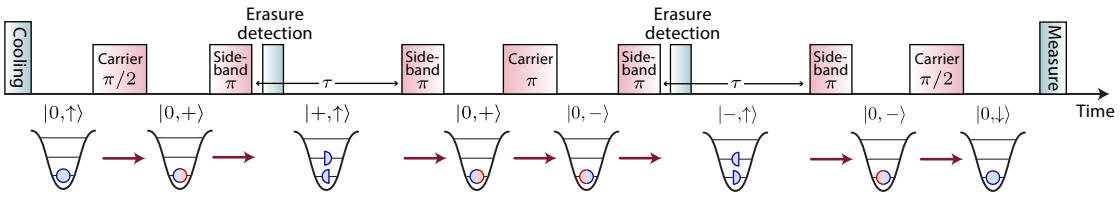

Fig. S5 | Motional-echo sequence. Sketch of the motional-echo sequence used in Fig. 3E, here assuming the phase accumulated during the wait time τ is exactly a multiple of 2π solely for presentation simplicity.

Scaling of P_{flip} and P_{same} with ω

We further comment on the scaling of P_{flip} and P_{same} with the trap frequency ω, in the sideband resolved ($\Omega \ll \omega$) and Lamb-Dicke ($\eta(2\bar{n}+1) \ll 1$) regimes. For simplicity, we will assume in the following that the atoms are initialized in the $|\downarrow\rangle$ state and that we drive a red sideband transition to the $|\uparrow\rangle$ state. Note that the results obtained below are also true if the atoms are initialized in $|\uparrow\rangle$.

Under these assumptions, P_{flip} to lowest order arises from off-resonant coupling via the $|0,\downarrow\rangle \rightarrow |1,\uparrow\rangle$ transition, with strength $\eta\Omega$ and detuning proportional to ω. We therefore obtain

$$P_{\text{flip}} \propto \frac{(\eta\Omega)^2}{\omega^2} \propto \frac{\Omega^2}{\omega^3},$$

where we used $\eta \propto 1/\sqrt{\omega}$.

P_{same} to lowest order arises from off-resonant coupling via the $|0,\downarrow\rangle \rightarrow |0,\uparrow\rangle$ transition, with strength $(1-\eta^2)\Omega \simeq \Omega$ and detuning proportional to ω. Once this off-resonant transition happens, the on-resonance red sideband transition $|0,\uparrow\rangle \rightarrow |1,\downarrow\rangle$ transfers the atoms back to the same spin state, but in a higher motional level. We therefore obtain

$$P_{\text{same}} \propto \frac{\Omega^2}{\omega^2}.$$

We can therefore extract the scaling of idealized sideband cooling and erasure correction cooling in the sideband resolved and deep Lamb-Dicke regimes. In particular, we obtain

$$1 - P_0^{\text{EC}} \propto \frac{\Omega^2}{\omega^2},$$

and

$$P_0^{\text{EC}} - P_0^{\text{SC}} \propto \frac{\Omega^2}{\omega^3}.$$

We verify these scalings using our numerical simulations results of idealized SC and ECC (Fig. S4C), which are also presented in Fig. 2F. We consider the ECC deficiency $1-P_0^{\text{EC}}$ (green solid line) as well as the difference between SC and ECC efficiencies $P_0^{\text{EC}} - P_0^{\text{SC}}$ (red solid line). In both cases, we fit our results with the function $f(\omega) = A(1/\omega)^B$ (dashed lines), where A and B are free parameters. The obtained exponents are $B = 1.9^{+1}_{-1}$ for $1 - P_0^{\text{EC}}$, and $B = 2.9^{+1}_{-1}$ for $P_0^{\text{EC}} - P_0^{\text{SC}}$. These results are consistent with the formulas derived above.

Motional coherence and motional-echo sequence

Here we describe the motional-echo sequence we use for the results presented in Fig. 3E. The sequence is similar to the one presented in Fig. 3A, and is further detailed in Fig. S5. In the absence of such an echo sequence, we find relatively short motional coherence times of up to ∼5 ms, limited by both trap frequency inhomogeneities within the array, and shot-to-shot fluctuations in trap frequency.

The scheme proceeds as follows: (1) we prepare the motion-superposition state $|+,\uparrow\rangle$ as described in the main text. (2) The state is then allowed to evolve for a duration τ. (3) We then convert the state back into the electronic manifold, and apply a carrier π-pulse, which exchanges the populations in $|\uparrow\rangle$ and $|\downarrow\rangle$. (4) The state is then transduced back into the motional manifold, meaning that effectively we have exchanged the populations in $|0\rangle$ and $|1\rangle$. (5) The state then evolves for time τ, realizing effectively a standard spin-echo sequence. Erasure-excision is performed on this sequence by performing a fast image just before steps (2) and (5), and post-selecting on detected atoms.

The motional-echo sequence used to obtain the results of Fig. 3E consists of four sideband pulses. In order to derive the one-way transduction fidelity $F_{\text{OW}} = 0.993^{+3}_{-3}$ quoted in the main text from the bare measured contrast of $F_{\text{tot}} = 0.972^{+10}_{-10}$, we assume that each sideband pulse is independent from the previous ones, meaning $F_{\text{tot}} = F_{\text{OW}}^4$. This assumption is reasonable as we perform erasure detection between sideband pulses, which both suppresses any potential coherent superposition between $|0,\downarrow\rangle$ and $|1,\uparrow\rangle$, and also ejects any atom left in $|\downarrow\rangle$.

Finally, we note that the fundamental limit to the motional coherence time would stem from Rayleigh scattering. This scattering rate was calculated[68] for the fermionic ^{87}Sr to be about $10^{-4}\,\text{s}^{-1}$ at a trap depth of a single recoil energy $U = E_r$; for comparison we typically operate at a trap depth of $U \approx 250E_r$ ($\approx 1300E_r$ during imaging).

Two qubit Rydberg gate

The controlled-Z (CZ) gate is realized by a global excitation in the Rydberg blockade regime with a time-optimal pulse[14,58,69,70]. We use a single-photon excitation to a Rydberg state ($5s61s\,^3S_1$) of two atoms spaced

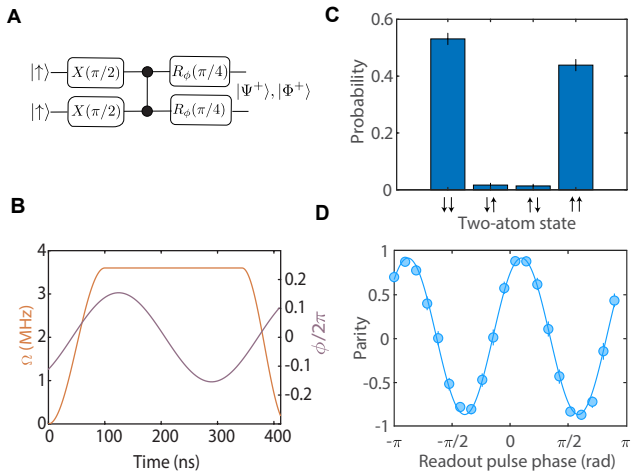

Fig. S6 | Two qubit Rydberg-mediated gate. A, Quantum circuit for preparation of a Bell-state in the electronic degree of freedom. **B,** The CZ gate is realized through single-photon excitation to a Rydberg state ($5s61s\ ^3S_1$) of two atoms spaced by 3.25 μm with a phase modulated field. **C,** Two-atom state population at the end of the circuit. We observe SPAM uncorrected 0.97^{+2}_{-2} population in the Bell-state Φ^+. **D,** Parity oscillations induced by final $\pi/2$ pulse with variable phase. We observe a contrast of 0.89^{+1}_{-1} with no SPAM correction.

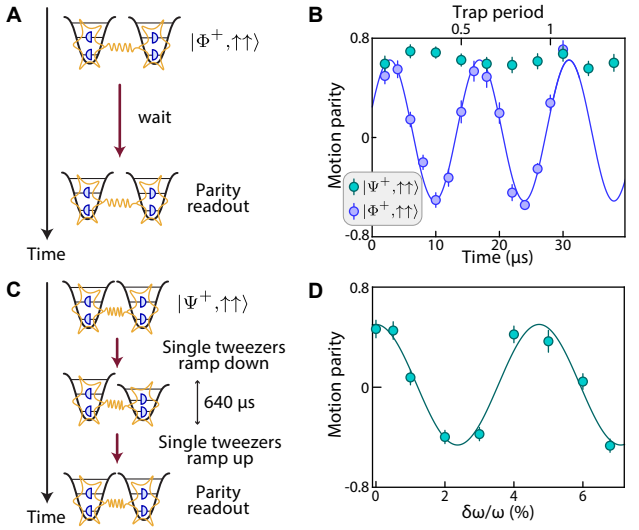

Fig. S7 | Inducing parity oscillations on an odd-parity Bell state with relative trap depth variation A, Sketch of the performed experiment to induce the parity oscillation on $|\Phi^+,\uparrow\uparrow\rangle$. **B,** Parity oscillations following the experiment described in **A** for $|\Phi^+,\uparrow\uparrow\rangle$ (also shown in Fig. 4B), and for $|\Psi^+,\uparrow\uparrow\rangle$, for which we do not observe significant oscillations. **C,** Sketch of the performed experiment to induce parity oscillations on $|\Psi^+,\uparrow\uparrow\rangle$. After preparing the motion-entangled Bell state $|\Psi^+,\uparrow\uparrow\rangle$, we ramp down the power of a single tweezer for a fixed duration of 640 μs. **D,** Motion parity as a function of the relative trap depth difference between the two tweezers.

by 3.25 μm with a phase modulated field (Fig. S6). A 500G magnetic field perpendicular to the $|\downarrow\rangle \rightarrow |\uparrow\rangle$ laser beam propagation axis is applied throughout the sequence, enabling high Rabi frequency on this transition. This high magnetic field results in a reduction of the Rydberg interaction strength as compared to low field conditions[71], and we leave an investigation of this effect to future work. We measure a C_6 coefficient of 52 GHz$\cdot\mu m^6$ and use a maximal Rabi frequency of $2\pi \times 3.6$ MHz.

The Bell states are produced as follows. Starting with both atoms in $|\downarrow\rangle$, we apply a first $\pi/2$ pulse on the $|\downarrow\rangle \rightarrow |\uparrow\rangle$ transition to prepare the superposition state $|+\rangle$. We then apply the CZ gate, and subsequently perform a $\pi/4$ pulse to obtain a Bell state. The choice of Bell state (either $|\Psi^+\rangle$ or $|\Phi^+\rangle$) is made by changing the phase of the last $\pi/4$ pulse. For $|\Phi^+\rangle$, we measure SPAM uncorrected populations $P_{\uparrow\uparrow}+P_{\downarrow\downarrow} = 0.97^{+2}_{-2}$; and induce parity oscillations with a final $\pi/2$ analyzing pulse where we measure a contrast of 0.89^{+1}_{-1}, yielding a SPAM-uncorrected optical Bell state[16] generation fidelity of 0.93^{+2}_{-2}.

We note that following further optimization, performed after the data for this manuscript was taken, we observe a SPAM-corrected controlled-Z fidelity > 0.99 in a randomized benchmarking sequence[14,58] (to be included in a different manuscript).

Parity oscillations for the motional Bell states

Here we show our results concerning parity oscillations of the odd-parity and even-parity motion-Bell states $|\Psi^+,\uparrow\uparrow\rangle = (|01\rangle + |10\rangle)/\sqrt{2} \otimes |\uparrow\uparrow\rangle$ and $|\Phi^+,\uparrow\uparrow\rangle = (|00\rangle + |11\rangle)/\sqrt{2} \otimes |\uparrow\uparrow\rangle$. After preparing these states, we perform the experimental sequence described in Fig. S7A, which consists of holding atoms in the motion Bell state for a variable amount of time, and then reading out the parity signal. We show the results of this experiment in Fig. S7B, for both $|\Phi^+,\uparrow\uparrow\rangle$ (blue circles) and $|\Psi^+,\uparrow\uparrow\rangle$ (green circles). We observe a significant difference in their behavior: for $|\Phi^+,\uparrow\uparrow\rangle$, we obtain a parity oscillation (also shown in Fig. 4B), whereas for $|\Psi^+,\uparrow\uparrow\rangle$, we do not observe significant parity oscillations.

This behavior is expected: as both tweezers have approximately the same power and same trap frequency ω, the energy spacing $\hbar\omega$ of the motional level is the same for both tweezers.

In order to prove that we undoubtedly prepare $|\Psi^+,\uparrow\uparrow\rangle$, we induce parity oscillations by varying the power of a single tweezer in the pair. The experimental sequence is described in Fig. S7C. After preparing the motion-entangled Bell state $|\Psi^+,\uparrow\uparrow\rangle$, we ramp down the power of a single tweezers for a fixed duration of $t_{\mathrm{wait}} = 640\,\mu$s. During this time, the state evolves as

$(|01\rangle + e^{i\delta\omega t_{\mathrm{wait}}}|10\rangle)/\sqrt{2} \otimes |\uparrow\uparrow\rangle$, where $\delta\omega$ is the trap frequency difference between the two tweezers.

After this step, we ramp up the tweezer power to its original value, and read-out the state's parity. We repeat this for various trap depth, and show our results as a function of $\delta\omega/\omega$ (Fig. S7B). We obtain a parity oscillation, indicating that we indeed prepared the $|\Psi^+, \uparrow\uparrow\rangle$ state.